inter.noise 2014
MELBOURNE AUSTRALIA
16-19 NOVEMBER

Bearing defect size estimation for extended raceway defects

Dick Petersen[1]; Carl Howard[2]

[1,2] The University of Adelaide, Australia

ABSTRACT

A method is presented for estimating the size of bearing raceway defects that are larger than the angular spacing between balls. Previous defect size estimation techniques cannot be used for such defects since they are limited to defects that are smaller than the ball angular spacing. The reason for this is that two defects that differ in size by the ball angular spacing produce the same time difference between the defect entrance and exit events in the vibration response, and it is this time difference that is used to estimate the defect size in previous techniques. Thus, to distinguish between such defects, a third feature of the vibration response is required. It is hypothesised and validated through simulations that the third distinguishing feature is the characteristic frequencies of the low frequency event. This event occurs when a ball gradually de- and restresses upon entering and exiting the defect and corresponds to a varying stiffness excitation of the rigid body modes of the bearing assembly. It is shown that two defects that differ in size by the ball angular spacing produce different rigid body modes because such defects generate different bearing stiffness variations. This results in low frequency events with different characteristic frequencies since these frequencies correspond to the natural frequencies of the rigid body modes that are excited as balls enter and exit the defect.

Keywords: Ball bearing, varying stiffness, defect, vibration, condition monitoring I-INCE Classification of Subjects Number: 41.3
(See http://www.inceusa.org/links/Subj%20Class%20-%20Formatted.pdf.)

1. INTRODUCTION

A number of bearing defect size estimation techniques have been developed (1, 2) which rely on estimating the time difference between the low and high frequency vibration events that occur as balls pass through a defect. The high frequency event occurs when a ball exits the defect and corresponds to an excitation of the high frequency bearing resonances. The low frequency event occurs when a ball gradually destresses upon entering the defect (3, 4) and corresponds to a varying stiffness (parametric) excitation of the rigid body modes of the bearing assembly (5). The previously developed defect size estimation techniques (1, 2) cannot distinguish between defects that differ in circumferential extent by (an integer times) the ball angular spacing since the time difference between the low and high frequency vibration events will be identical for such defects. To distinguish between such defects when estimating their size, a third feature of the vibration response is therefore required. This paper hypothesises that under the same static loading conditions, the third feature is the characteristic frequency of the low frequency event. This hypothesis is validated by simulating the vibration response for such defects using a previously developed multi-body nonlinear dynamic model of a defective rolling element bearing (1, 5).

2. MULTI-BODY NONLINEAR DYNAMIC MODEL OF A DEFECTIVE BEARING

2.1 Model diagram

Figure 1 presents a diagram of the multi-body nonlinear dynamic model of a ball bearing with an outer raceway defect. The deep-groove ball bearing considered here has N_b balls, a pitch radius R_p, a ball radius R_b, and an unloaded contact angle $\alpha_0 = 0°$. Only radial displacements and bearing stiffness variations are considered because the ball bearing is radially loaded which results in a loaded contact angle $\alpha = 0°$. The inner raceway and shaft are modelled as a single rigid body of mass m_i and its displacement is defined by $x_i(t)$ and $y_i(t)$. The outer raceway and bearing support structure are modelled as a single rigid body of mass m_o and its displacements is defined by $x_o(t)$ and $y_o(t)$. The radial stiffness and damping of the bearing support

[1] dick.petersen@adelaide.edu.au
[2] carl.howard@adelaide.edu.au

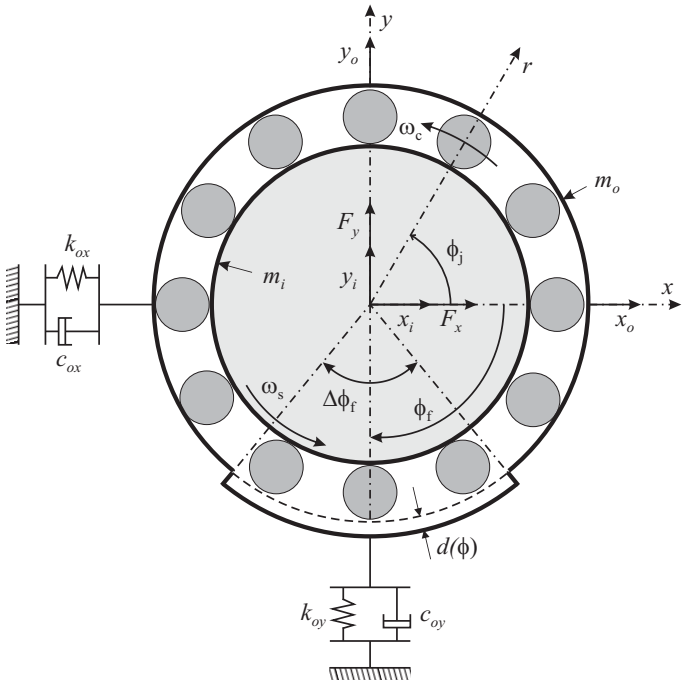

Figure 1 – Multi-body nonlinear dynamic model of a radially loaded defective ball bearing. The bearing has a square-shaped outer raceway defect of depth $d(\phi)$ and circumferential extent $\Delta\phi_f$ which is centred at ϕ_f.

structure are modeled by the parameters k_{ox}, k_{oy}, c_{ox} and c_{ox}. The bearing is subjected to a static radial load $\mathbf{F}$ defined by

$$\mathbf{F} = [F_x \quad F_y]^{\mathrm{T}}, \tag{1}$$

where F_x and F_y are the x and y components of the static radial load. Further details of the model can be found in Refs. (5, 6). The high-frequency bearing resonance that was included in the model presented in Refs. (5, 6) is excluded here because the emphasis is on the varying stiffness excitation of the rigid body modes of the bearing assembly.

2.2 Bearing macro-geometry and kinematics

The shaft in Figure 1 rotates at a run speed $\omega_s = 2\pi f_s$ which results in a nominal cage speed $\omega_c = 2\pi f_c$ of

$$\omega_c = \frac{\omega_s}{2}\left(1 - \frac{R_b \cos\alpha}{R_p}\right). \tag{2}$$

The angular position $\phi_j(t)$ of ball j shown in Figure 1 is defined as

$$\phi_j(t) = \phi_c(t) + \frac{2\pi(j-1)}{N_b}, \quad j = 1 \text{ to } N_b, \tag{3}$$

with $\phi_c(t)$ the cage angular position and N_b the number of balls. Equation (3) defines the cage angular position to coincide with ball $j = 1$. For the case of an outer raceway defect considered here, the nominal defect frequency is given by the outer raceway ball pass frequency

$$f_{bpo} = N_b f_c. \tag{4}$$

Slippage of the balls is considered in the model by including small variations in the cage speed $\phi_c(t)$ as described in Refs. (5, 6).

2.3 Defect depth profile

In the diagram of the bearing shown in Figure 1, the outer raceway defect has a circumferential extent defined by $\Delta\phi_f$ and is centred at an angle ϕ_f. The defect location ϕ_f is constant for an outer raceway defect but rotates at the shaft speed ω_s for an inner raceway defect, such that $\phi_f(t) = \phi_f(0) + \omega_s t$. The study presented here considers square-shaped outer raceway defects of depth h for which a defect depth profile $d(\phi)$ is

generated as

$$d(\phi) = \begin{cases} \min\left(h, R_b^2 - \sqrt{R_b^2 - 0.25R_o^2(\phi - \phi_f + 0.5\Delta\phi_f)^2}\right) & \text{if} \quad \phi_f - 0.5\Delta\phi_f \le \phi < \phi_f \\ \min\left(h, R_b^2 - \sqrt{R_b^2 - 0.25R_o^2(\phi_f + 0.5\Delta\phi_f - \phi)^2}\right) & \text{if} \quad \phi_f < \phi \le \phi_f + 0.5\Delta\phi_f \\ 0 & \text{if} \quad \phi_f + 0.5\Delta\phi_f \le \phi \le \phi_f - 0.5\Delta\phi_f \end{cases} \tag{5}$$

where $R_o = R_p + R_b + c/2$ is the outer raceway radius. Equation (5) effectively describes the path of the centre of the ball as it traverses the square-shaped defect (6). Defects with more complicated defect depth profiles, such as extended defects with significant surface waviness features, can be generated as described in Refs. (5, 7). Figure 3(f) presents example defect depth profiles for square-shaped defects of depth $h = 50$ μm and circumferential extents $\Delta\phi_f = 20$ and 60°, with the solid and dashed lines indicating the modeled and actual defect depth profiles, respectively.

2.4 Hertzian contact deformations and forces

The relative displacements between the inner and outer raceways are contained in a vector $\mathbf{q}(t)$ which is defined as

$$\mathbf{q}(t) = [\delta_x(t) \quad \delta_y(t)]^{\mathrm{T}} = [x_i(t) - x_o(t) \quad y_i(t) - y_o(t)]^{\mathrm{T}}, \tag{6}$$

where $\delta_x(t)$ and $\delta_y(t)$ are the relative displacements in the x and y directions, respectively. The Hertzian contact deformation $\delta_j(t)$ for ball j is given by

$$\delta_j(t) = \delta_x(t)\cos\phi_j(t) + \delta_y(t)\sin\phi_j(t) - c - d(\phi_j(t)), \tag{7}$$

where $d(\phi_j(t))$ is the defect depth profile evaluated at the ball angular position $\phi_j(t)$, and c is the radial clearance. The Hertzian contact force $Q_j(t)$ associated with the contact deformation $\delta_j(t)$ is defined by the load-deflection relationship

$$Q_j(t) = K\delta_j^+(t)^{1.5}, \tag{8}$$

where the load-deflection factor K (units of $\mathrm{N/m^{1.5}}$) depends on the curvatures and material properties of the surfaces in contact (8). The contact force $Q_j(t)$ acts in the radial direction. The superscript $(\cdot)^+$ indicates that $\delta_j(t)$ is set to zero when it is smaller than zero.

2.5 Nonlinear equations of motion

The nonlinear equations of motion are now given by (5)

$$\mathbf{M}\ddot{\mathbf{x}}(t) + \mathbf{C}\dot{\mathbf{x}}(t) + \mathbf{K}\mathbf{x}(t) + \sum_{j=1}^{N_b}[k_j(t)\delta_j^+(t) + c\dot{\delta}_j(t)]\mathbf{R}_j(t) = \mathbf{F}, \tag{9}$$

where the state vector $\mathbf{x}(t)$ is given by

$$\mathbf{x}(t) = \begin{bmatrix} x_i(t) & y_i(t) & x_o(t) & y_o(t) \end{bmatrix}^{\mathrm{T}}. \tag{10}$$

The nonlinear spring stiffness $k_j(t)$ in Equation (9) models the Hertzian contact stiffness for ball j and is defined as

$$k_j(t) = K\sqrt{\delta_j^+(t)}. \tag{11}$$

The matrix $\mathbf{R}_j(t)$ in Equation (9) defines a transformation from orthogonal to radial coordinates and is formulated as

$$\mathbf{R}_j(t) = \begin{bmatrix} \cos\phi_j(t) & \sin\phi_j(t) & -\cos\phi_j(t) & -\sin\phi_j(t) \end{bmatrix}^{\mathrm{T}}. \tag{12}$$

The mass, stiffness and damping matrices in Equation (9) are defined as

$$\mathbf{M} = \begin{bmatrix} \mathbf{M}_i & \mathbf{0} \\ \mathbf{0} & \mathbf{M}_o \end{bmatrix} \quad \mathbf{K} = \begin{bmatrix} \mathbf{0} & \mathbf{0} \\ \mathbf{0} & \mathbf{K}_o \end{bmatrix} \quad \mathbf{C} = \begin{bmatrix} \mathbf{0} & \mathbf{0} \\ \mathbf{0} & \mathbf{C}_o \end{bmatrix}, \tag{13}$$

with

$$\mathbf{M}_i = \begin{bmatrix} m_i & 0 \\ 0 & m_i \end{bmatrix} \quad \mathbf{M}_o = \begin{bmatrix} m_o & 0 \\ 0 & m_o \end{bmatrix} \quad \mathbf{K}_o = \begin{bmatrix} k_{ox} & 0 \\ 0 & k_{oy} \end{bmatrix} \quad \mathbf{C}_o = \begin{bmatrix} c_{ox} & 0 \\ 0 & c_{oy} \end{bmatrix}. \tag{14}$$

3. FORMULATION OF VARYING STIFFNESS OF A DEFECTIVE BALL BEARING

3.1 Load distribution

For a defective ball bearing subjected to static radial load $\mathbf{F}$ defined in Equation (1), static equilibrium is achieved when the sum of the loads generated by the static contact forces $\bar{Q}_j$ over all balls equals the applied static loads. Using Equations (7) and (8), the loads carried by the balls are thus found by solving the following set of nonlinear algebraic equations as a function of the cage angular position ϕ_c

$$\begin{bmatrix} F_x \\ F_y \end{bmatrix} = \sum_{j=1}^{N_b} \bar{Q}_j \begin{bmatrix} \cos\phi_j \\ \sin\phi_j \end{bmatrix} = \sum_{j=1}^{N_b} \begin{bmatrix} F_{xj} \\ F_{yj} \end{bmatrix}. \tag{15}$$

A Newton-Raphson method can be used to solve Equation (15) at each considered cage angular position, with the ball positions ϕ_j depending on the cage angular position as defined by Equation (3). The bearing relative displacements that solve Equation (15) are defined as

$$\bar{\mathbf{q}} = [\bar{\delta}_x \quad \bar{\delta}_y]^{\mathrm{T}}. \tag{16}$$

Once the relative displacements $\bar{\mathbf{q}}$ are solved as a function of the cage angular position, the corresponding contact deformations are calculated using Equations (7) and (8), with solutions denoted by $\bar{(\cdot)}$ similar to Equation (16). For a defect-free bearing, the solutions are found by solving Equation (15) while setting $d(\phi) = 0$.

3.2 Bearing stiffness variations

The bearing stiffness variations are calculated by linearising the force-displacement relationship defined by Equations (7) and (8) at the relative displacements and rotations $\bar{\mathbf{q}}$ that solve Equation (15). The resulting symmetric bearing stiffness matrix $\mathbf{K}_b$ is defined as (5)

$$\mathbf{K}_b = \begin{bmatrix} k_{xx} & k_{xy} \\ k_{xy} & k_{yy} \end{bmatrix} = \begin{bmatrix} \frac{\partial F_x}{\partial \delta_x} & \frac{\partial F_x}{\partial \delta_y} \\ \frac{\partial F_y}{\partial \delta_x} & \frac{\partial F_y}{\partial \delta_y} \end{bmatrix}_{\mathbf{q}=\bar{\mathbf{q}}} = 1.5K \sum_{j=1}^{N_b} \sqrt{\bar{\delta}_j^+} \begin{bmatrix} \cos^2\phi_j & \cos\phi_j \sin\phi_j \\ \cos\phi_j \sin\phi_j & \sin^2\phi_j \end{bmatrix}. \tag{17}$$

Each element of the stiffness matrix $\mathbf{K}_b$ varies with cage angular position even for the case of a defect-free bearing for which $d(\phi) = 0$, leading to the well-known varying stiffness vibrations (9, 10). However, a raceway defect typically causes much larger and faster stiffness variations compared to a defect-free bearing, and may also reduce the average stiffness over a single cage rotation, especially when multiple balls are in the defect at once. This will be demonstrated by the simulations presented in Section 4.

3.3 Linearised multi-body dynamic model

The nonlinear dynamic model defined by Equation (9) is now linearised at the quasi-static displacements $\bar{\mathbf{q}}$, which are calculated as described in Section 3.1, and the natural frequencies and damping ratios of the modes of the resulting linearised system are defined. The linearised equations of motion are given by

$$\mathbf{M}\ddot{\bar{\mathbf{x}}}(t) + \bar{\mathbf{C}}\dot{\bar{\mathbf{x}}}(t) + \bar{\mathbf{K}}\bar{\mathbf{x}}(t) = \mathbf{0}, \tag{18}$$

where $\bar{\mathbf{x}}(t) = \mathbf{x}(t) - \bar{\mathbf{x}}$ are small displacements around the quasi-static solution $\bar{\mathbf{x}}$. This solution is calculated as described in Section 3.1 by noting that $\bar{y}_o = F_y/k_{oy}$, $\bar{x}_o = F_x/k_{ox}$, $\bar{y}_i = \bar{y}_o + \bar{\delta}_y$, and $\bar{x}_i = \bar{x}_o + \bar{\delta}_x$. The linearised stiffness and damping matrices in Equation (18) are formulated as

$$\bar{\mathbf{K}} = \begin{bmatrix} \mathbf{K}_b & -\mathbf{K}_b \\ -\mathbf{K}_b & \mathbf{K}_b + \mathbf{K}_o \end{bmatrix}, \quad \bar{\mathbf{C}} = \begin{bmatrix} \mathbf{C}_b & -\mathbf{C}_b \\ -\mathbf{C}_b & \mathbf{C}_b + \mathbf{C}_o \end{bmatrix}, \tag{19}$$

where the damping matrix $\mathbf{C}_b$ is formulated as (5)

$$\mathbf{C}_b = \begin{bmatrix} c_{xx} & c_{xy} \\ c_{xy} & c_{yy} \end{bmatrix} = c \sum_{j=1}^{N_b} \begin{bmatrix} \cos^2\phi_j & \cos\phi_j \sin\phi_j \\ \cos\phi_j \sin\phi_j & \sin^2\phi_j \end{bmatrix}. \tag{20}$$

The bearing stiffness matrix $\mathbf{K}_b$ in Equation (17) is calculated as described in Section 3.2 and varies with cage angular position ϕ_c as well as the circumferential extent $\Delta\phi_f$ of the defect. The viscous contact damping constant c in Equation (9) is adjusted such that the bearing damping terms c_{xx} and c_{yy} in Equation (20) for the defect-free case (normalised by 1 Ns/m) are in the order of 0.25-2.5 $\times 10^{-5}$ times the linear bearing stiffness terms k_{xx} and k_{yy} (normalised by 1 N/m), respectively (11).

3.4 Rigid body modes of linearised dynamic model

The undamped natural frequencies ω_n and damping ratios ζ_n of the modes of the linearised dynamic system defined by Equation (18) are calculated by solving the following generalized eigenvalue problem (12)

$$\begin{bmatrix} \mathbf{0} & -\bar{\mathbf{K}} \\ -\mathbf{M} & \mathbf{0} \end{bmatrix} \mathbf{v} = -\lambda \begin{bmatrix} \mathbf{M} & \bar{\mathbf{C}} \\ \mathbf{0} & \mathbf{M} \end{bmatrix} \mathbf{v}. \tag{21}$$

This results in eight eigenvalues λ_n (four complex conjugate pairs) and eigenvectors $\mathbf{v}_n$ from which the undamped natural frequencies and damping ratios are calculated as

$$\omega_n = |\lambda_n|, \quad \zeta_n = \frac{|\mathrm{Re}(\lambda_n)|}{|\lambda_n|}, \quad n = 1, 2, \ldots, 8. \tag{22}$$

These natural frequencies vary periodically at the ball pass frequency due to the varying bearing stiffness $\mathbf{K}_b$, and are also dependent on the circumferential extent $\Delta\phi_f$ of the defect as demonstrated in the next section.

4. SIMULATION RESULTS

4.1 Model implementation

The deep-groove ball bearing considered here has $N_b = 9$ balls, a ball radius $R_b = 3.97$ mm, a pitch radius $R_p = 19.66$ mm, an unloaded contact angle $\alpha_0 = 0^\circ$, and a radial clearance $c = 0$ μm. The bearing is subjected to a radial load $F_y = -400$ N in the vertical direction while the horizontal component $F_x = 0$ N. The bearing has a square-shaped outer raceway defect of depth $h = 50$ μm centred in the load zone at $\phi_f = 270^\circ$. The two modeled defects have circumferential extents of $\Delta\phi_f = 20^\circ$ and 60° such that they exactly differ in size by the ball angular spacing of $360^\circ/N_b = 40^\circ$. The multi-body nonlinear dynamic model was implemented in Simulink® and the equations of motion were solved using the ordinary differential equation solver (ode45) which is based on a Runga-Kutta method. The running speed was set to $f_s = 20$ Hz which results in a nominal outer raceway defect frequency $f_{bpo} = N_b f_c = 71.8$ Hz. Initial conditions were set to the static displacements $\bar{\mathbf{x}}$ corresponding to the cage position at time $t = 0$. The continuous time-domain results were discretized using a sample frequency $F_s = 32,768$ Hz and acceleration spectra were calculated from 2.1 seconds of simulated data using a Hanning window and a frequency resolution of 128 Hz. The other parameter values used in the model are included in Table 1.

Table 1 – Parameter values used in the multi-body nonlinear dynamic model of the defective ball bearing.

Hertzian contacts	Mass	Stiffness	Damping
$K = 7.93$ GN/m$^{1.5}$	$m_i = 0.3$ kg	$k_{ox} = 740.2$ kN/m	$c_{ox} = 47.1$ Ns/m
	$m_o = 0.3$ kg	$k_{oy} = 740.2$ kN/m	$c_{oy} = 47.1$ Ns/m

4.2 Load distribution for defective ball bearing

Figure 2 presents the load distribution for the two defect circumferential extents of $\Delta\phi_f = 20^\circ$ and 60°. The load distribution for a defect-free bearing is indicated by the green line, and the gray-shaded rectangles indicate the circumferential extent of the defects. The number of balls positioned in the defect zone at any one time varies between none or one for $\Delta\phi_f = 20^\circ$ and one or two for $\Delta\phi_f = 60^\circ$. Figure 2 shows that when a ball is positioned in the defect, it destresses and loses its load carrying capacity and the load it carried is redistributed to the balls outside the defect zone. Defect-free raceway sections are thus subjected to increased static loading when balls lose their load carrying while traversing through the defect. In general, the load carrying capacity that is lost and the associated load redistribution will depend mostly on the defect geometry, but also on the applied load and the radial clearance. When the defect circumferential extent $\Delta\phi_f$ is smaller than the ball angular spacing of 40°, the load distribution only deviates from the defect-free case when a single ball is in the defect zone, as shown in Figure 2(a). When the defect grows larger than the ball angular spacing such that $\Delta\phi_f > 40^\circ$, multiple balls are in the defect at once and the load distribution deviates entirely from the defect-free case, as shown in Figure 2(b). For this case, there is a large increase in the load carried by the balls located outside the defect zone. As shown in the next section, the redistribution of the load results in large variations of the effective stiffness of the bearing assembly due to the nonlinear nature of the Hertzian contact stiffness, which becomes stiffer as the contact force $\bar{Q}_j$ becomes larger.

4.3 Rigid body modes of linearised dynamic system

Figure 3(a–e) compares the radial stiffness variations $\mathbf{K}_b$ and the corresponding variations in the natural frequencies ω_n of the rigid body modes of the defective bearing assembly, for the two considered defects with

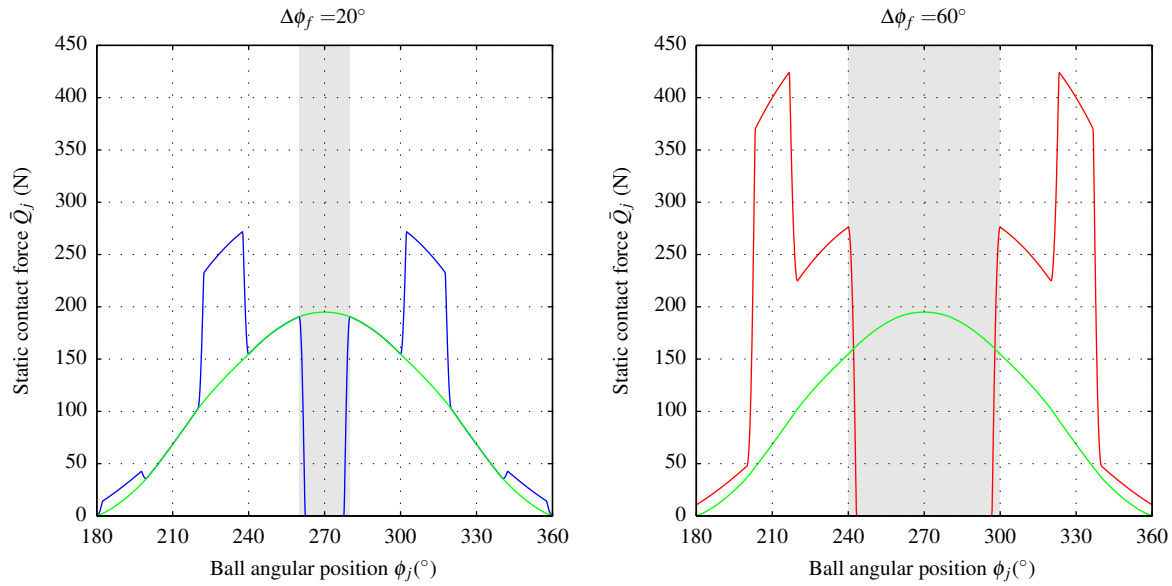

Figure 2 – Load distribution for a defect-free bearing (*green*) and a defective bearing with a square-shaped outer raceway defect of depth $h = 50$ μm centred at $\phi_f = 270°$ with circumferential extents of (*a*) $\Delta\phi_f = 20°$ and (*b*) $\Delta\phi_f = 60°$. The gray-shaded rectangles indicate the circumferential extent of the defect.

circumferential extents of $\Delta\phi_f = 20°$ and $60°$ as well as the defect-free case. The corresponding defect depth profiles $d(\phi)$ are presented in Figure 3(f). The bearing stiffness and natural frequencies of the rigid body modes vary periodically with the fundamental period defined by the ball angular spacing of 40°. Figure 3(e) shows that the radial cross-coupling stiffness k_{xy} is much smaller than the radial stiffnesses k_{xx} and k_{yy} presented in Figure 3(a) and (c). As a result, analysis of the eigenvectors $\mathbf{v}_n$ for each of the four rigid body modes shows that two modes have dominant motion in the x direction and two in the y direction. The corresponding natural frequencies of these modes have been labelled as ω_{x1}, ω_{x2}, ω_{y1}, and ω_{y2} and their variation with cage position ϕ_c is presented in Figure 3(b) and (d). The results in these figures illustrate that defects with circumferential extents that differ by the ball angular spacing produce different variations in the natural frequencies of the rigid body modes. The mean natural frequencies ω_{y1} and ω_{y2} are lower for the larger defect with $\Delta\phi_f = 60°$ because the mean radial stiffness k_{yy} is lower compared to the smaller defect with $\Delta\phi_f = 20°$, as shown in Figure 3(c). The mean natural frequencies ω_{x1} and ω_{x2} are higher for the larger defect because the mean radial stiffness k_{xx} is larger in Figure 3(a). As demonstrated in the next section, this results in low frequency entrance and exit events in the simulated vibration response that have different characteristic frequencies.

4.4 Simulated vibration response

Figure 4(a–d) present the simulated vibration responses in the horizontal and vertical directions for the considered defects with circumferential extents $\Delta\phi_f = 20°$ and $60°$. A short time segment is shown to illustrate a single defect entrance and exit event in the vibration response. Since a high frequency bearing resonance was not included in the model, the simulated results do not contain the high frequency event that normally occurs in conjunction with a low frequency event when a balls exits the defect. Figure 4(e) and (f) present the contact forces for the balls that enter and exit the defect within the time segment shown, with the thin lines indicating the static contact forces $\bar{F}_{xj}$ and $\bar{F}_{yj}$, which were calculated as described in Section 3.1, and the thick lines indicating the dynamic contact forces $F_{xj}(t)$ and $F_{yj}(t)$, which fluctuate around and decay to the static contact forces as balls enter and exit the defect.

For the smaller defect with $\Delta\phi_f = 20°$, Figure 4(a) and (c) show that the horizontal vibration response has a lower amplitude than the vertical vibration response. This occurs because the bearing assembly is predominantly excited in the y direction due to the locations of the defect entrance and exit, and this excitation does not produce significant rigid body motion in the x direction since the radial cross-coupling stiffness k_{xy} is small as was observed in Figure 3(e). For the larger defect with $\Delta\phi_f = 60°$, Figure 4(b) and (d) show that the amplitudes of the horizontal and vertical vibration responses are more similar because the bearing assembly is excited in both the x and y directions due to the larger extent of the defect.

For the shorter defect with $\Delta\phi_f = 20°$, the contact forces presented in Figure 4(e) show that the entrance and exit events are caused by a single ball ($j = 9$) de- and restressing between the raceways as it traverses

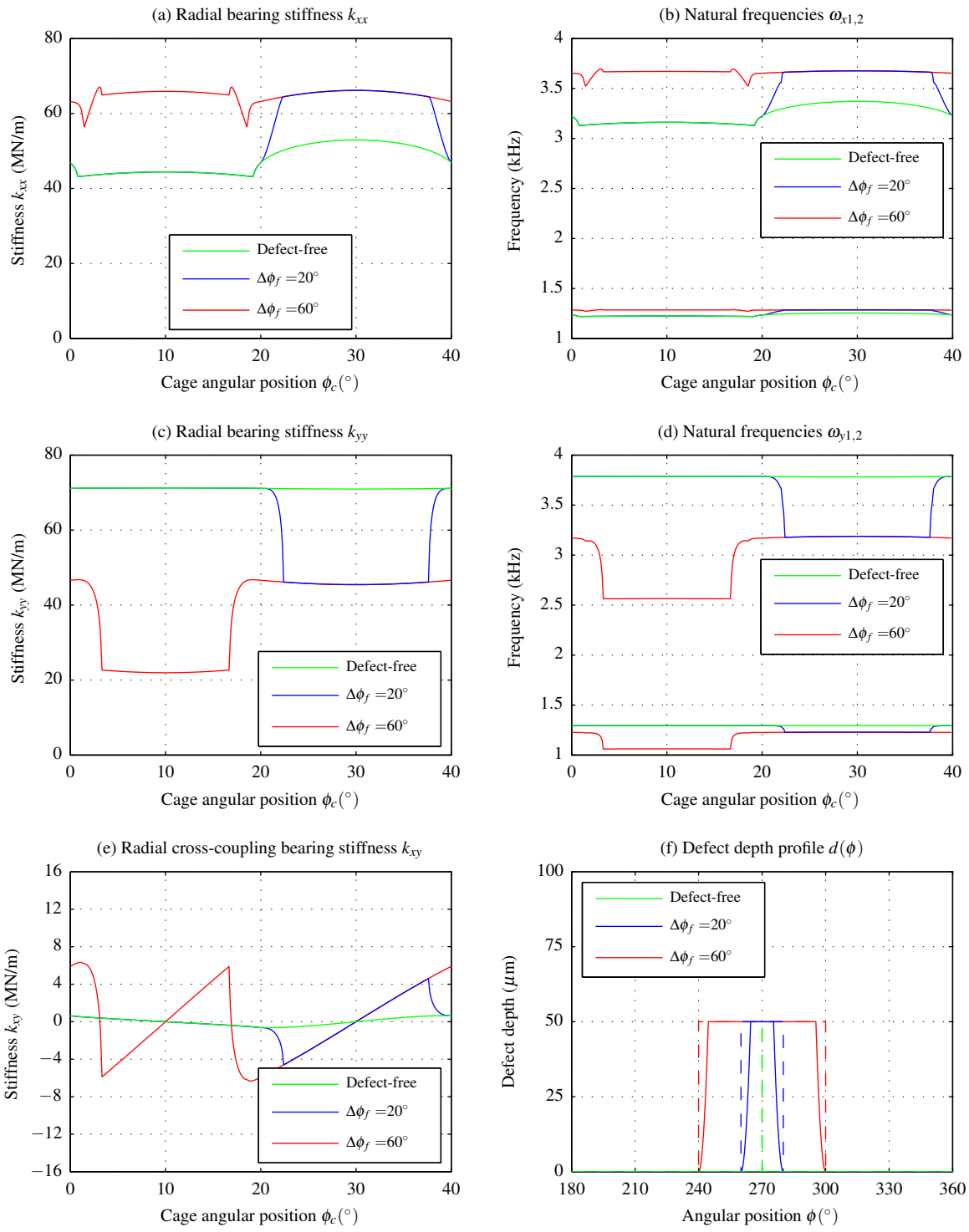

Figure 3 – Variations in bearing stiffness and natural frequencies of the rigid body modes of the linearised dynamic system for the case of a square-shaped outer raceway defect of depth $h = 50$ μm and circumferential extent $\Delta\phi_f = 20°$ and 60° centred at $\phi_f = 270°$. (*a*) Radial bearing stiffness k_{xx}. (*b*) Natural frequencies of modes with dominant motion in *x*-direction. (*c*) Radial bearing stiffness k_{yy}. (*d*) Natural frequencies of modes with dominant motion in *y*-direction. (*e*) Radial cross-coupling bearing stiffness. (*f*) Modeled (*solid*) and actual (*dashed*) defect depth profiles.

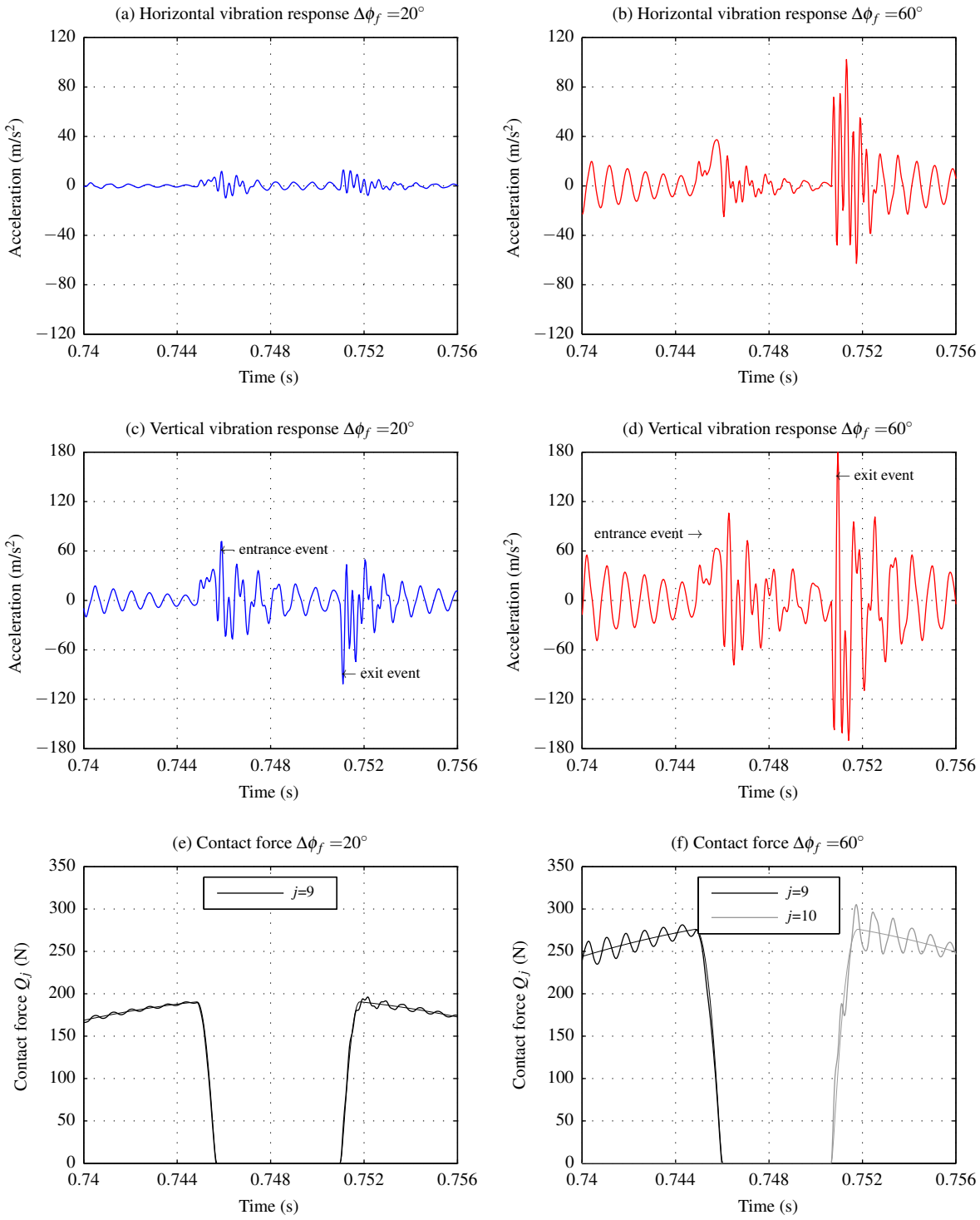

Figure 4 – Simulated vibration response and contact forces for the case of a square-shaped outer raceway defect of depth $h = 50$ μm and circumferential extent $\Delta\phi_f = 20°$ and 60° centred at $\phi_f = 270°$. (*a*) Horizontal acceleration for $\Delta\phi_f = 20°$. (*b*) Horizontal acceleration for $\Delta\phi_f = 60°$. (*c*) Vertical acceleration for $\Delta\phi_f = 20°$. (*d*) Vertical acceleration for $\Delta\phi_f = 60°$. (*e*) Contact force $Q_j(t)$ for ball $j = 9$ (thick line) passing through defect with $\Delta\phi_f = 20°$ with thin line indicating the static load solution $\bar{Q}_j$. (*f*) Contact forces $Q_j(t)$ (thick lines) for balls entering ($j = 9$) and exiting ($j = 10$) defect with $\Delta\phi_f = 60°$ with thin lines indicating the static load solution $\bar{Q}_j$.

through the defect. For the larger defect with $\Delta\phi_f = 60°$, Figure 4(f) shows that the entrance and exit events are caused by two different balls; one ball ($j = 9$) destresses as it enters the defect and another ball ($j = 10$) restresses between the raceways as it exits. The time difference $\Delta t = \text{mod}(\Delta\phi_f, 40°)/\omega_c = 0.007$s between the entrance and exit events is the same for both defects because the circumferential extents of the two defects differ by the ball angular spacing of 40°. The simulated results thus illustrate that a third feature is required to distinguish between the two defects when estimating their size. The next section demonstrates that this third feature is the characteristic frequencies of the low frequency entrance and exit events.

4.5 Characteristics of low frequency entrance and exit events

Figure 5 presents the spectral densities of the simulated vibration responses and illustrates that the third feature that can be used to distinguish between the two defects is the difference in the characteristic frequencies of the low frequency events. The dashed lines indicate the minimum and maximum values of the natural frequencies ω_{x1}, ω_{x2}, ω_{y1} and ω_{y2} of the rigid body modes of the bearing assembly vary, which were illustrated in Figure 3(b) and (d).

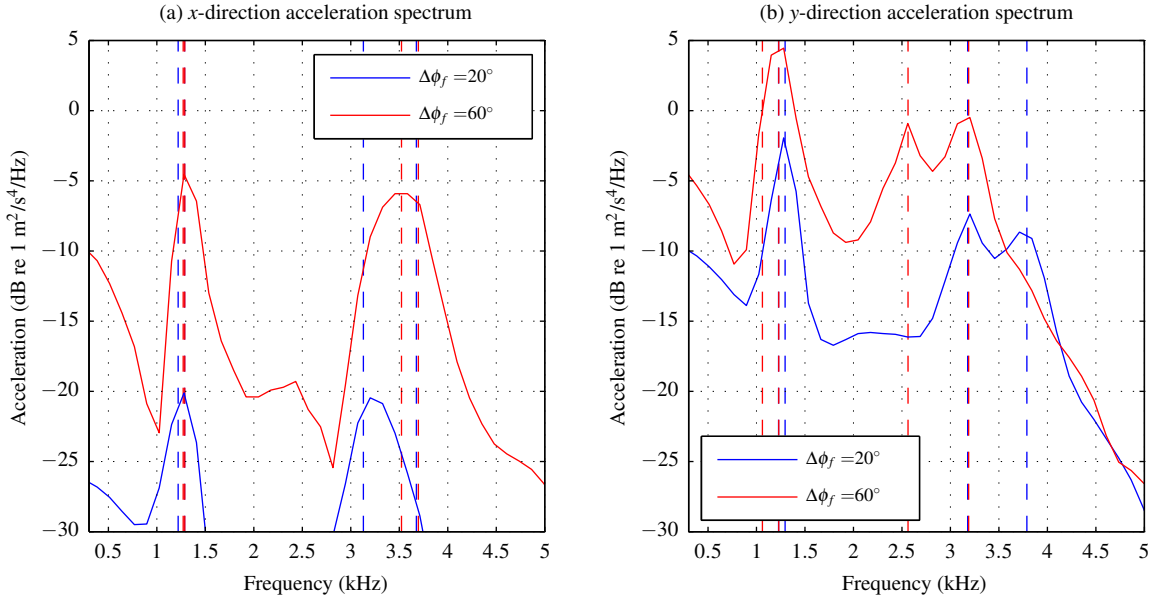

Figure 5 – Simulated vibration spectra for a square-shaped outer raceway defect of depth $h = 50$ μm and circumferential extents of $\Delta\phi_f = 20°$ and $\Delta\phi_f = 60°$. (*a*) Horizontal vibration response with the dashed lines indicating the minimum and maximum values of ω_{x1} and ω_{x2}. (*b*) Vertical vibration response with the dashed lines indicating the minimum and maximum values of ω_{y1} and ω_{y2}.

Figure 5(a) shows that as the defect grows in size from $\Delta\phi_f = 20°$ to 60°, the characteristic frequencies of the low frequency events in the horizontal vibration response increase which correlates to the variations in the natural frequencies ω_{x1} and ω_{x2} observed in Figure 3(b). For the vertical vibration response, Figure 5(b) shows that the characteristic frequencies of the low frequency event decrease as the defect grows which correlates to the variations in the natural frequencies ω_{y1} and ω_{y2} observed in Figure 3(b). Thus, the shifting of the characteristic frequencies of the low frequency events observed in the vibration spectra can be used to distinguish between the two defects when estimating their size.

5. CONCLUSION

The presented simulation results demonstrate that the characteristic frequency of the low frequency events observed in the vibration response, which are caused by varying stiffness excitations of the rigid body modes that occur when balls enter and exit the defect (5), changes with the size of the defect. This means that the characteristic frequencies of the low frequency event can be used as a feature in defect size estimation techniques in order to overcome the inability of current techniques (1, 2) to distinguish between defects that differ in size by the ball angular spacing. Experimental work will need to be undertaken to further validate this hypothesis.

ACKNOWLEDGEMENT

The work presented in the paper was funded by Australian Research Council (ARC) Linkage Project LP110100529.

REFERENCES

1. Sawalhi N, Randall RB. Vibration response of spalled rolling element bearings: Observations, simulation and signal processing techniques to track the spall size. Mechanical Systems and Signal Processing. 2011;25:846–870.

2. Zhao S, Liang L, Xu G, Wang J, Zhang W. Quantitative diagnosis of a spall-like fault of a rolling element bearing by empirical mode decomposition and the approximate entropy method. Mechanical Systems and Signal Processing. 2013;40(1):154–177.

3. Moazen Ahmadi A, Petersen D, Howard C. A nonlinear dynamic vibration model of defective bearings - The importance of modelling the finite size of rolling elements. Accepted in Mechanical Systems and Signal Processing. 2014 June;.

4. Singh S, Köpke UG, Howard CQ, Petersen D. Analyses of contact forces and vibration response for a defective rolling element bearing using an explicit dynamics finite element model. Article in Press in the Journal of Sound and Vibration. 2014;.

5. Petersen D, Howard C, Sawalhi N, Moazen Ahmadi A, Singh S. Analysis of bearing stiffness variations, contact forces and vibrations in radially loaded double row rolling element bearings with raceway defects. Article in Press in Mechanical Systems and Signal Processing. 2014;.

6. Sawalhi N, Randall RB. Simulating gear and bearing interactions in the presence of faults Part I: The combined gear bearing dynamic model and the simulation of localised bearing faults. Mechanical Systems and Signal Processing. 2008;22:1924–1951.

7. Sawalhi N, Randall RB. Simulating gear and bearing interactions in the presence of faults Part II: Simulation of the vibrations produced by extended bearing faults. Mechanical Systems and Signal Processing. 2008;22:1952–1966.

8. Harris TA, Kotzalas MN. Rolling Bearing Analysis - Essential Concepts of Bearing Technology. 5th ed. CRC Press; 2006.

9. Liew H, Lim TC. Analysis of time-varying rolling element bearing characteristics. Journal of Sound and Vibration. 2005;283:1163–1179.

10. Sunnersjö CS. Varying compliance vibrations of rolling bearings. Journal of Sound and Vibration. 1978;58(3):363–373.

11. Sopanen J, Mikkola A. Dynamic model of a deep-groove ball bearing including localized and distributed defects. Part 1: Theory. Journal of Multi-body Dynamics. 2003;217:201–211.

12. Gunduz A, Dreyer JT, Singh R. Effect of bearing preloads on the modal characteristics of a shaft-bearing assembly: Experiments on double row angular contact ball bearings. Mechanical Systems and Signal Processing. 2012;31:176–195.